Front. Phys. 13(2), 136501 (2018)
https://doi.org/10.1007/s11467-017-0743-1

RESEARCH ARTICLE

# Structural, optical, and thermal properties of MAX-phase $Cr_2AlB_2$

**Xiao-Hong Li**[1,2,3,†], **Hong-Ling Cui**[1], **Rui-Zhou Zhang**[1]

[1] *College of Physics and Engineering, Henan University of Science and Technology, Luoyang 471023, China*
[2] *Department of Chemistry, Nanjing University of Science and Technology, Nanjing 210094, China*
[3] *Henan Key Laboratory of Photoelectric Energy Storage Materials and Applications, Luoyang 471023, China*
*Corresponding author. E-mail:* †*lorna639@yeah.net*

*Received May 23, 2017; accepted July 20, 2017*

First-principles calculations of the structural, optical, and thermal properties of $Cr_2AlB_2$ are performed using the pseudopotential plane-wave method within the generalized gradient approximation (GGA). Calculation of the elastic constant and phonon dispersion indicates that $Cr_2AlB_2$ is mechanically and thermodynamically stable. Analysis of the band structure and density of states indicates that $Cr_2AlB_2$ is metallic. The thermal properties under increasing temperature and pressure are investigated using the quasi-harmonic Debye model. The results show that anharmonic effects on $Cr_2AlB_2$ are important at low temperature and high pressure. The calculated equilibrium primitive cell volume is 95.91 Å$^3$ at $T = 300$ K, $P = 0$ GPa. The ability of $Cr_2AlB_2$ to resist volume changes becomes weaker with increasing temperature and stronger with increasing pressure. Analysis of optical properties of $Cr_2AlB_2$ shows that the static dielectric function of $Cr_2AlB_2$ is 53.1, and the refractive index $n_0$ is 7.3. If the incident light has a frequency exceeding 16.09 eV, which is the plasma frequency of $Cr_2AlB_2$, $Cr_2AlB_2$ changes from metallic to dielectric material.

**Keywords** electronic structure, optical properties, first-principles calculations, $Cr_2AlB_2$, thermal properties

**PACS numbers** 65.80.-g, 65.40.Ba, 61.50.Ah

## 1 Introduction

The MAX phases are a group of hexagonal-structure compounds with the common formula $M_{n+1}AX_n$ (where M is an early transition metal, A stands for an A group element, X represents C and/or N, and $n = 1$–$3$). MAX phases crystallize in the $P6_3/mmc$ space group, and stacks of near-close-packed $M_6X$ octahedral layers are interleaved with a single layer of pure element A [1]. This nanolaminated structure produces a unique combination of the advantages of metals and ceramics, because the layered structure consists of a hard carbide or nitride part $(MX)_n$ with variable thickness and a ductile intermetallic part MA [1, 2]. MAX phases exhibit the desirable properties of metals (good thermal and electrical conduction, machinability, and thermal shock resistance) and ceramics (good resistance to chemical attack, oxidation, and creep); therefore, they have potential applications in industries such as energy generation, chemical processing, and medicine [2].

Jeitschko [3, 4] discovered the $M_2AlB_2$-type (space group $C_{mmm}$) and MAlB-type (space group $C_{mcm}$) ternary transition metal borides; their structures are analogous to the MAX phases with one or two Al layers interleaving the transition metal boride sublattice. Early transition metal borides are among the hardest and highest-melting compounds, and binary borides such as $ReB_2$ were found to have higher hardness because of strong covalent bonding between boron atoms and strong repulsion between the core electrons of the early transition metal [5]. Rogl [6] showed that the structures of borides are based on trigonal prisms. The structure of CrB was determined to be parallel and congruent [7], and combinations of polygons beyond hexagons appears, for example, in $YCrB_4$ [8]. Then Kuz'ma *et al.* [9] determined the crystal structure of the ternary boride $Cr_2AlB_2$. A single crystal of $Cr_2AlB_2$ was investigated in 2015 [10]. To the best of our knowledge, little experimental and theoretical information about the electronic, optical, and thermal properties of $Cr_2AlB_2$ is available. Thus, it is necessary to investigate these properties theoretically to best exploit them for further industrial applications.

The projector augmented wave (PAW) method is an efficient method to investigate periodic systems. In this work, the PAW method is used to calculate the structural, electronic, optical, and thermal properties of $Cr_2AlB_2$, which are then compared with the available experimental values. Density functional theory (DFT) within the quasi-harmonic approximation was used to provide a reasonable description of the thermal properties below the melting point of bulk materials [11, 12]. The thermal expansion, heat capacity, isothermal bulk modulus, etc. are investigated. Some optical properties such as the dielectric properties, refractivity, and conductivity are also calculated using the B3LYP (Becke, three-parameter, Lee–Yang–Parr) hybrid functional. These calculations can provide useful reference data for experimentalists, and our work will be a good starting point for further theoretical and experimental work on this compound.

## 2 Computational details

$Cr_2AlB_2$ has an orthorhombic crystal structure under standard pressure (1 bar) and crystallizes in the $Cmmm$ space group [10]. Energy and electronic structure calculations have been conducted under the generalized gradient approximation (GGA) of DFT in the framework of the PAW method and a plane-wave basis set [13] as implemented in the Vienna *ab-initio* simulation package (VASP) [14]. The B3LYP [15] hybrid functional was used. Geometric optimization of the unit cell and atomic positions were performed using the conjugate gradient algorithm with a plane-wave cutoff energy of 700 eV. In the optimization process, the $k$-point sampling in the Brillouin zone was $9\times9\times9$ and was based on the Monkhorst–Pack method to ensure energy convergence with energy differences of less than 1 meV per atom.

The band structure and electronic density of states (DOS) were also calculated. To obtain the electronic DOS, the tetrahedron method with Bloch corrections was used for Brillouin zone integration, and a dense sampling grid of $15 \times 15 \times 15$ $k$ points was used.

The optical properties are among the most important properties of a material and can be determined using the dielectric function, $\varepsilon(\omega) = \varepsilon_1(\omega) + \mathrm{i}\varepsilon_2(\omega)$, in the linear response range. A dense sampling grid of $15 \times 15 \times 15$ $k$ points was used to calculate the optical properties. The real part $\varepsilon_1(\omega)$ and imaginary part $\varepsilon_2(\omega)$ can be obtained by calculating the wave function matrix. On the basis of the dielectric function, other optical properties such as the refractive index $n(\omega)$, extinction coefficient $k(\omega)$, optical reflectivity $R(\omega)$, absorption coefficient $\alpha(\omega)$, and energy-loss spectrum $L(\omega)$ can be obtained [16]. The theoretical formulas for these optical properties are as follows [17, 18]:

$$\varepsilon_2(\omega) = \frac{\pi}{\varepsilon_0}\left(\frac{e}{m\omega}\right)^2 \times \sum_{V,C}\left\{\int_{\mathrm{BZ}}\frac{2\mathrm{d}K}{(2\pi)^3}|a\cdot M_{CV}(K)|^2 \times\delta[E_C(K)-E_V(K)-\hbar\omega]\right\}, \tag{1}$$

$$\varepsilon_1(\omega) = 1+\frac{2e}{\varepsilon_0 m^2}\sum_{V,C}\left\{\int_{\mathrm{BZ}}\frac{2\mathrm{d}K}{(2\pi)^3}\frac{|a\cdot M_{CV}(K)|^2}{[E_C(K)-E_V(K)]} \times\frac{\hbar^3}{[E_C(K)-E_V(K)]^2-\hbar^2\omega^2}\right\}, \tag{2}$$

$$n(\omega) = \frac{1}{\sqrt{2}}[\sqrt{\varepsilon_1(\omega)^2+\varepsilon_2(\omega)^2}+\varepsilon_1(\omega)]^{\frac{1}{2}}, \tag{3}$$

$$k(\omega) = \frac{1}{\sqrt{2}}[\sqrt{\varepsilon_1(\omega)^2+\varepsilon_2(\omega)^2}-\varepsilon_1(\omega)]^{\frac{1}{2}}, \tag{4}$$

$$R(\omega) = \frac{[n(\omega)-1]^2+k^2(\omega)}{[n(\omega)-1]^2-k^2(\omega)}, \tag{5}$$

$$a(\omega) = \frac{2\omega k(\omega)}{c} = \frac{\varepsilon_2(\omega)\omega}{n(\omega)c}, \tag{6}$$

$$L(\omega) = \frac{\varepsilon_2(\omega)}{\varepsilon_1(\omega)^2+\varepsilon_2(\omega)^2}, \tag{7}$$

where $C$ and $V$ represent the conduction band and valence band, respectively. BZ is the first Brillouin zone, $K$ is the reciprocal lattice, and $E_C(K)$ and $E_V(K)$ are the intrinsic energy levels of the conduction band and valence band, respectively. $|a\cdot M_{CV}(K)|^2$ is the matrix element of the momentum transition, $\varepsilon_0$ is the vacuum permittivity, $a$ is the unit direction vector, and $\omega$ is the angular frequency.

The thermodynamic function was fitted to the integral form of the Vinet equation of state (EOS) at zero pressure [19]. The Helmholtz free energy and Gibbs free energy were obtained from the minimum values of the thermodynamic functions at finite temperatures, whereupon the equilibrium volume and bulk moduli were obtained through the EOS. The heat capacity $C_p$ was determined by a numerical differentiation $\frac{\partial V}{\partial T}$ and by polynomial fitting of both $C_v$ and $S$.

The supercell approach and force-constant method were used to calculate the phonon dispersion. The real space force constants of the supercells were calculated by density functional perturbation theory, and the phonon modes were calculated from the force constants using the PHONOPY package [20]. A $3\times1\times3$ supercell including 90 atoms with a $13 \times 7 \times 13$ $k$ mesh was used to ensure convergence.

## 3 Results and discussion

### 3.1 Structural properties

The $Cr_2AlB_2$ crystal is an orthogonal system with space group *Cmmm*. Its unit cell contains two unit formulas. Figure 1 shows its crystal structure, and the total energy versus the volume is plotted in Fig. 2. By fitting the data of the total energy and the volume to Murnaghan's equation of state [21], the equilibrium lattice volume, bulk modulus $B_0$, and pressure derivative of the bulk modulus $B_0'$ can be obtained. Table 1 lists the lattice constants and structural parameters of $Cr_2AlB_2$; the available experimental values are also given.

The calculated lattice constants in Table 1 agree well with the experimental values of 2.9373, 11.0513, and 2.9675 Å for $a$, $b$, and $c$, respectively, although the calculated values are slightly underestimated. The differences between the calculated and experimental values of the lattice constants are 0.39%, 0.08%, and 1.04% for $a$, $b$, and $c$, respectively. The $B_1$–$B_4$ bond length is 1.7610 Å, which is close to the experimental value of 1.7616 Å [10]. These $B_1$–$B_4$ bonds form a zigzag chain with a B–B–B bond angle of 112.6°, which is close to the experimental value of 113.0°. In addition, the $B_1$–$B_4$ bond is longer than the B–B bonds of $Cr_3AlB_4$ (1.739 Å) and $Cr_4AlB_6$ (1.738 Å) [10]. This indicates that the B–B bond length increases with increasing boron content. Similarly, the lengths of the other bonds, such as $Cr_1$–$B_3$, $Cr_1$–$B_2$, $Cr_1$–$Cr_2$, and $Al_1$–$B_1$, are all close to the corresponding experimental values [10].

To understand the structural stability, we further investigated the elastic constants of $Cr_2AlB_2$ using the CASTEP program [22]. Table 2 lists the calculated elastic constants $C_{ij}$ (GPa), bulk modulus $B$ (GPa), shear modulus $G$ (GPa), Young's modulus $E$ (GPa), $G/B$ ratio, Poisson's ratio $v$, and Vicker's hardness $H_v$ (GPa) at ambient pressure. The available experimental values are also given.

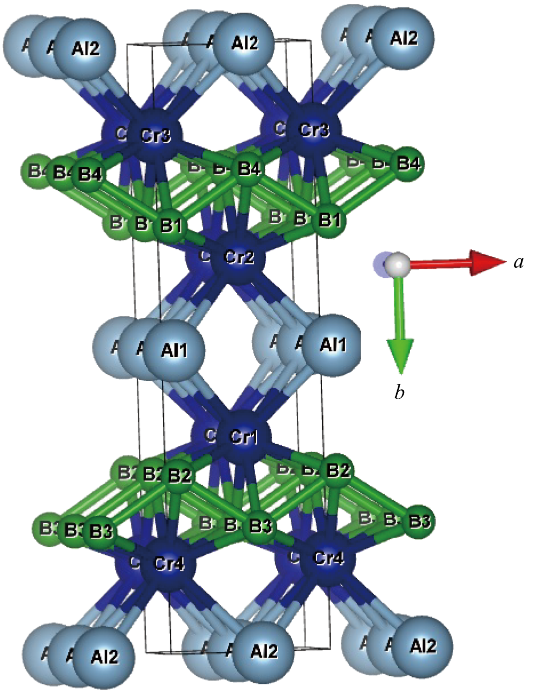

**Fig. 1** Crystal structure and molecular numbering of *Cmmm* $Cr_2AlB_2$.

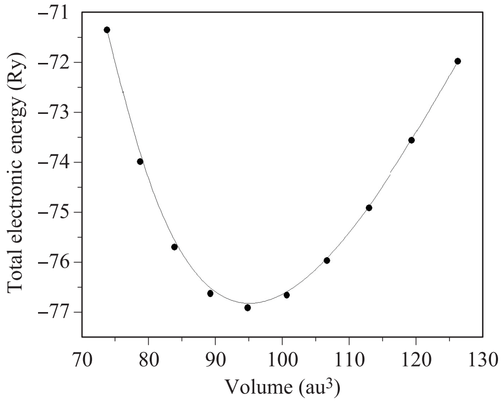

**Fig. 2** Graph of total energy versus volume.

**Table 1** Experimental and calculated lattice constants, atomic positions, bond lengths, and angles of *Cmmm* $Cr_2AlB_2$ crystal at standard pressure.

| Atom | $(x, y, z)_{\text{calculated}}$ | $(x, y, z)_{\text{expt*}}$ |
|---|---|---|
| Cr | $(0.5000, 0.6478, 0.0000)$ | $(0.5000, 0.6478, 0.0000)$ |
| Al | $(0.0000, 0.5000, 0.5000)$ | $(0.0000, 0.5000, 0.5000)$ |
| B | $(0.0000, 0.2942, 0.5000)$ | $(0.0000, 0.2942, 0.50000)$ |

| Bond length (Å) | | Bond angle (°) | |
|---|---|---|---|
| $B_1$–$B_4$ | 1.7610 (1.7616) | $B_1$–$B_3$–$B_1$ | 112.6 (113.0)* |
| $Cr_1$–$B_3$ | 2.1985 (2.2014) | $Cr_1$–$B_3$–$Cr_4$ | 76.3 |
| $Cr_1$–$B_2$ | 2.1853 (2.1876) | $Cr_2$–$Al_1$–$Cr_1$ | 76.4 |
| $Cr_1$–$Al_1$ | 2.6382 (2.6443) | $Al_1$–$Cr_1$–$Al_1$ | 67.3 |
| $Cr_1$–$Cr_2$ | 3.2647 (3.2460) | $B_2$–$Cr_1$–$B_3$ | 103.7 |
| $Al_1$–$B_1$ | 2.2727 (2.2765) | $Al_1$–$Cr_1$–$B_2$ | 55.4 |

Lattice constants

$a = 2.9256$ Å (2.9373 Å)*, $b = 11.0422$ Å (11.0513 Å)
$c = 2.9365$ Å (2.9675 Å), $V = 69.95$ Å$^3$ (96.33 Å$^3$)

Note: *The values in parentheses are experimental values taken from Ref. [10].

**Table 2** Calculated elastic constants $C_{ij}$ (GPa), bulk modulus $B$ (GPa), shear modulus $G$ (GPa), Young's modulus $E$ (GPa), $G/B$ ratio, Poisson's ratio $\nu$, and Vicker's hardness $H_\nu$ (GPa) at ambient pressure, compared with available experimental and theoretical results.

| $C_{11}$ | $C_{22}$ | $C_{33}$ | $C_{44}$ | $C_{55}$ | $C_{66}$ | $C_{12}$ | $C_{13}$ | $C_{23}$ |
|---|---|---|---|---|---|---|---|---|
| 457 | 397 | 414 | 156 | 199 | 164 | 89 | 89 | 100 |
| B | G | E | G/B | $\nu$ | $H_\nu^{\mathrm{Equ(9)}}$ | $H_\nu^{\mathrm{B4C}}$ | $H_\nu^{\mathrm{c\text{-}BN}}$ | $H_\nu^{\mathrm{Diamond}}$ |
| 202 | 169 | 397 | 0.83 | 0.17 | 29.6 | $31.7^a$ | $65.2^a$ $(66)^a$ | $95.7^a$ $(96)^a$ |

Note: The values in parentheses are experimental values, and the values outside of parentheses are computational values.
[a] The values are taken from Ref. [23].

The elastic constants of orthorhombic systems have nine independent components, and the necessary conditions for mechanical stability are given by [24]

$$\begin{aligned} &C_{11}+C_{22}+C_{33}+2C_{12}+2C_{13}+2C_{23}>0,\\ &C_{22}+C_{33}-2C_{23}>0,\\ &C_{ii}>0 \quad (i=1\text{–}6). \end{aligned} \tag{8}$$

From Table 2, the entire set of elastic constants $C_{ij}$ satisfies the mechanical stability criteria [24], which shows that the studied structure is mechanically stable at ambient pressure. The bulk modulus is attributed mainly to the valence-electron density of transition metals [25]. For $Cr_2AlB_2$, the calculated bulk modulus is 202 GPa, which is close to the fitted value (209 GPa) from the Birch–Murnaghan EOS. The shear modulus and Poisson's ratio [26] ($K = G/B$) are two important elastic properties that are thought to be related to the hardness on the basis of the empirical formulation of Chen *et al.* [27]. For polycrystalline materials, the hardness can be written as

$$H_\nu = 2(K^2G)^{0.585} - 3. \tag{9}$$

Using Eq. (9), the hardness of $Cr_2AlB_2$ is estimated to be 29.6 GPa. For comparison, the hardness values of $B_4C$, c-BN, and diamond are also listed in Table 2; all are larger than that of $Cr_2AlB_2$. The hardness of $Cr_2AlB_2$ is intermediate between those of other materials with similar structures such as W–Ru–B ($H_v$: $\sim$ 17 GB) [28] and $W_{45.6}Re_{30.4}B_{24}$ ($H_v$: 23.5 GPa) [29]. The boron content is not necessarily the factor that determines whether a material is hard or superhard [30]. The low hardness of $Cr_2AlB_2$ may be attributed to its low shear strength [25]. Note that the calculated $C_{11}$ value is larger than the calculated $C_{22}$ and $C_{33}$ values, which indicates that the resistance to deformation along the $a$ direction is stronger than that along the $c$ and $b$ directions. One possible explanation for the large value of $C_{11}$ may be related to the deformation of more B–B units along the $a$-axis direction than along the $b$- and $c$-axis directions.

### 3.2 Electronic properties

To confirm the dynamical stability of $Cr_2AlB_2$, the phonon dispersion curve is calculated at standard pressure and presented in Fig. 3. A dynamically stable crystal structure requires that all phonon frequencies be positive; otherwise, the structure will be dynamically unstable [31]. The absence of imaginary frequencies in the entire Brillouin zone confirms the dynamical stability of $Cr_2AlB_2$ at standard pressure.

The DOS and partial density of states (PDOS) of $Cr_2AlB_2$ are shown in Fig. 4. $Cr_2AlB_2$ has a large finite DOS of 5.70 states/eV at the Fermi energy level, which confirms its metallic nature. The DOS near the Fermi level consists mainly of Cr 3d orbital electrons, with some B 2p orbital electrons and negligible contributions from Al 2p states. Few electrons are available from the s orbital near the Fermi energy level. Figure 5 shows the calculated band structures of $Cr_2AlB_2$ along the high-symmetry directions of the Brillouin zone. The overlap between the conduction and valence bands again confirms its metallic nature. This suggests that $Cr_2AlB_2$, like other MAX phases, would exhibit metallic conductivity.

From Fig. 5, the Fermi energy ($E_F$) is crossed by five different bands, one along the Γ–Z direction and the other four along the Γ–X direction, indicating metallic behavior along the directions parallel to the $a$ and $c$ axes. Further, buckling along the $b$ axis opens band gaps of 0.72 and 0.28 eV along the X–S and Y–Γ directions, respectively. Thus, $Cr_2AlB_2$ behaves as a metal with strong anisotropy. Further, the electrical conductivity is confined along the $a$ and $c$ directions.

### 3.3 Thermal properties

The thermal properties of materials can provide information about the phase stability, melting point, strength, types of bonds, etc. In this paper, the thermodynamic properties of $Cr_2AlB_2$ at different temperatures are further investigated using the quasi-harmonic Debye model.

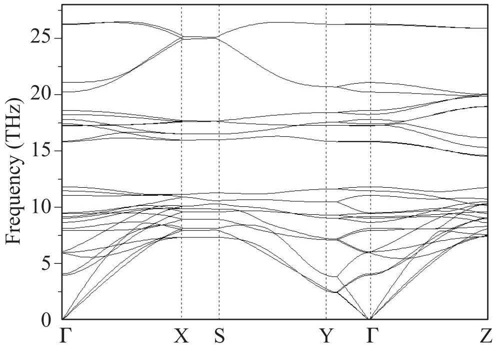

**Fig. 3** Phonon dispersion curves of *Cmmm* $Cr_2AlB_2$.

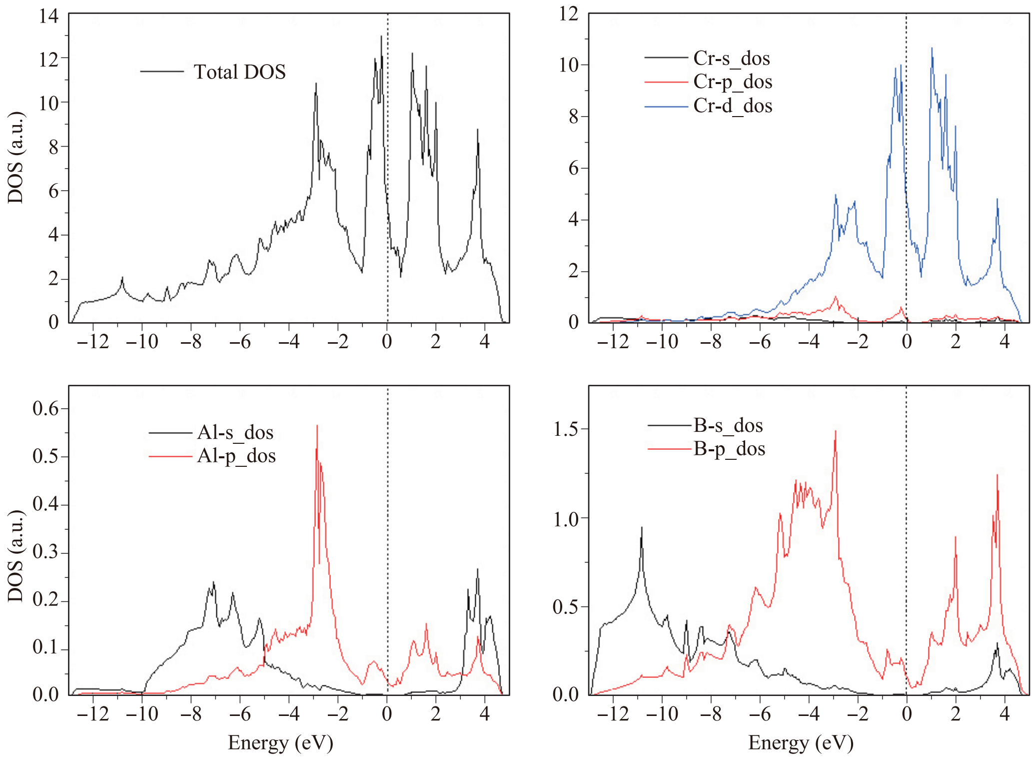

**Fig. 4** Total electronic DOS and PDOS of $Cr_2AlB_2$.

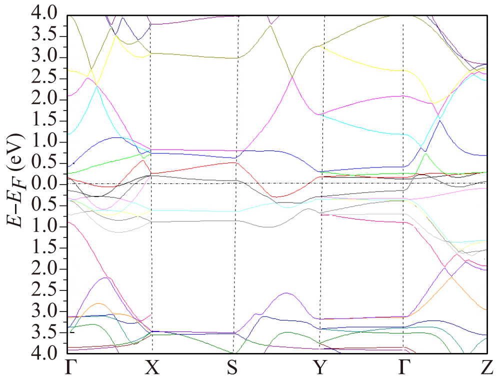

**Fig. 5** Electronic band structures of $Cr_2AlB_2$.

The calculated data for the total energy versus primitive cell volume ($E$–$V$) are first obtained in the static approximation and then fitted with a numerical EOS to determine the structural parameters at $P = 0$ and $T = 0$. Then the macroscopic properties as functions of temperature and pressure are obtained from the standard thermodynamic relations. The thermal properties are studied at pressures ranging from 0 to 100 GPa and temperatures up to 2000 K. Figure 6 shows the effect of the temperature and pressure on the primitive cell volume.

Note that the volume increases linearly with increasing temperature. The rate of increase is nearly zero from 0 to 150 K and becomes very moderate for $T > 150$ K. In addition, the volume decreases with increasing pressure for a given temperature. At $T = 300$ K and $P = 0$ GPa, the calculated equilibrium primitive cell volume $V$ is 95.91 $Å^3$. Figure 7 shows the relationship between the bulk modulus $B$ and the temperature at different pressures. The bulk modulus is nearly constant for $T < 150$ K and then decreases linearly with increasing temperature. In addition, the bulk modulus increases with increasing pressure at a given temperature. This indicates that the ability of $Cr_2AlB_2$ to resist volume changes be-

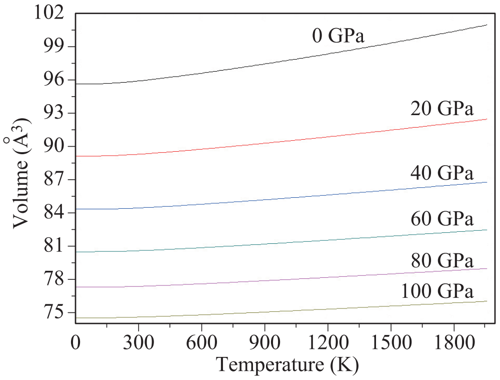

**Fig. 6** Variation of primitive cell volume as a function of temperature.

comes weaker with increasing temperature and stronger with increasing pressure. At $T = 300$ K and $P = 0$ GPa, the bulk modulus is 240.7 GPa.

The heat capacity is an important parameter in condensed matter physics and can provide essential insight into a material's vibrational properties. Figure 8 shows the variation of the heat capacity $C_v$ versus temperature. Note that $C_v$ increases sharply and is proportional to $T^3$ at very low temperature [32]. At higher temperature, $C_v$ follows the Debye model and tends to the Dulong–Petit limit [33], which is approximately given by the classic equipartition law $C_v = 3Nk_B$, where $N$ is the number of atoms of the considered system, and $k_B$ is the Boltzmann constant. In addition, $C_v$ decreases gradually with increasing pressure for a given temperature. Further, the effect of temperature on $C_v$ is more significant than that of pressure. To the best of our knowledge, no experimental data have been reported for the heat capacity $C_v$. The $C_v$ value of $Cr_2AlB_2$ at zero pressure and 300 K is 213.2.

The anharmonicity is restricted to the thermal expansion within the quasi-harmonic approximation. As the thermal expansion coefficient exhibits anharmonic behavior, one cannot expect linear variations with temperature and pressure. Figure 9 shows the effect of temperature and pressure on the thermal expansion coefficient $\alpha$. Note that $\alpha$ first increases quickly with increasing temperature up to 500 K. Then $\alpha$ tends to increase linearly at temperatures above 500 K. This shows that anharmonic effects are important at low temperature and high pressure for $Cr_2AlB_2$, and the effect of the temperature on $\alpha$ is very small at high temperature. With increasing pressure, $\alpha$ decreases sharply for a given temperature. Further, the thermal expansion decreases more rapidly as the temperature increases. At $T = 300$ K and $P = 0$ GPa, $\alpha$ is $2.13 \times 10^{-5}$ $K^{-1}$.

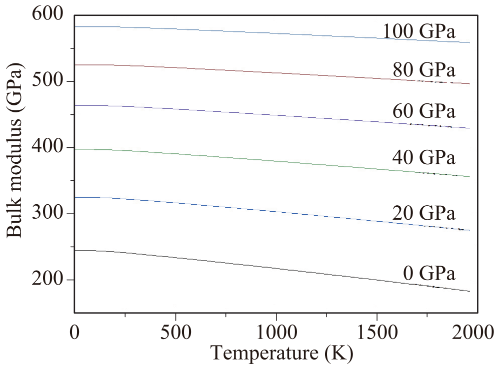

**Fig. 7** Temperature-dependence of bulk modulus $B$ of $Cr_2AlB_2$ at different pressures.

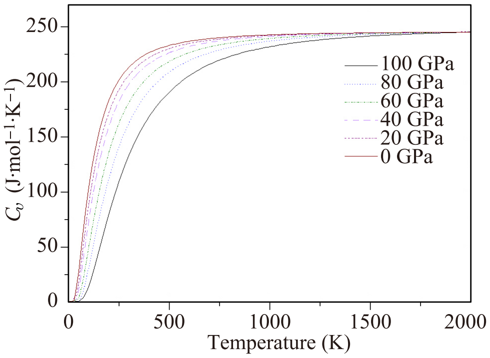

**Fig. 8** Calculated temperature-dependence of heat capacity of $Cr_2AlB_2$ at constant volume.

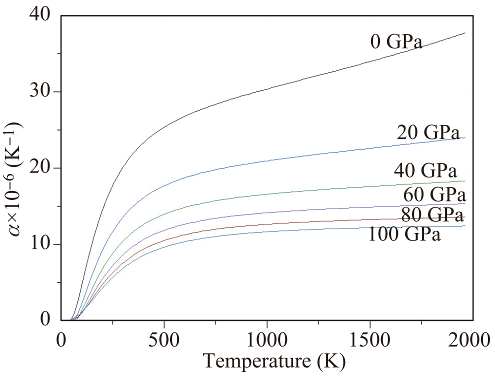

**Fig. 9** Variation of the thermal expansion coefficient as a function of temperature and pressure.

### 3.4 Optical properties

The dielectric function describes the effect of an electric field such as an oscillating light wave on a material [34]. $\varepsilon_1(\omega)$ provides information on the electronic polarizability of the material [30]. The peak of the imaginary part $\varepsilon_2(\omega)$ is related to the electron excitation. Figure 10(a) shows the dielectric function of $Cr_2AlB_2$ as a function of photon energy. Note that $\varepsilon_1(\omega)$ decreases sharply with increasing photon energy when the photon energy is small, reaching a minimum at a photon energy of 3.03 eV. When the photon energy is larger than 3.03 eV, $\varepsilon_1(\omega)$ first increases and then decreases to the minimum at a photon energy of 8.33 eV. At higher photon energies, $\varepsilon_1(\omega)$ shows steady behavior at the high-energy limit. Thus, $Cr_2AlB_2$ is transparent to high-energy radiation.

When the photon energy ranges from 2.66 to 3.54 eV and 4.8 to 16.08 eV, $\varepsilon_1(\omega) < 0$, and $Cr_2AlB_2$ exhibits metallic characteristics. From the vector wave equation, $\omega^2\varepsilon = c^2(K \cdot K)$, the vector wave $K$ is an imaginary number when $\varepsilon_1(\omega) < 0$. This shows that light cannot propagate in this frequency range. The static dielectric constant $\varepsilon_1(0)$ is approximately 53.1, which is much larger than those of $BaTiO_3$ (5.12), $BiInO_3$ (6.75), and $Ti_3N_4$ (18.31) [35–38]. This shows that $Cr_2AlB_2$ is a promising dielectric material and useful in the manufacture of high-value capacitors [39]. From Fig. 10(a), $\varepsilon_2(\omega)$ first increases and then decreases with increasing photon energy. The photon energy for the first dielectric peak of $\varepsilon_2(\omega)$, which is generated by charge transfer between the Cr 3d and B 2p states, is 1.88 eV. $\varepsilon_2(\omega)$ reaches a second peak value at 4.79 eV, which corresponds to the transition derived from charge transfer between the Cr 3d and B 2p states. When a material is transparent, $\varepsilon_2(\omega)$ is zero, but it becomes nonzero when absorption begins. The $\varepsilon_2(\omega)$ value of $Cr_2AlB_2$ is zero at approximately 16 eV, which indicates that $Cr_2AlB_2$ becomes transparent above 16 eV.

Figure 10(b) shows the refractive index $n$ and extinction coefficient $k$ of $Cr_2AlB_2$. Note that $n$ and $k$ show trends that are similar to those of the real and imaginary parts of the dielectric function, respectively. The refractive index $n_0$ is maximum for the entire photon energy range and is 7.3, which is found to satisfy the condition $n_0 = \sqrt{\varepsilon_1(0)}$. As the value of $n$ is greater than 1, photons entering the material are slowed by interactions with electrons in the material. The extinction coefficient $k$ reaches a peak at a photon energy of 2.4 eV and decreases to zero when the photon energy is approximately 16.2 eV. This indicates that the intrinsic oscillation frequency of $Cr_2AlB_2$ is approximately 16.2 eV, and $Cr_2AlB_2$ is transparent in the ultraviolet. At photon energies of 2.66 to 3.54 eV and 4.82 to 16.09 eV, the extinction coefficient $k$ is larger than the refractive index $n$, indicating that light cannot propagate in these ranges, and $Cr_2AlB_2$ exhibits the reflective behavior of a metal.

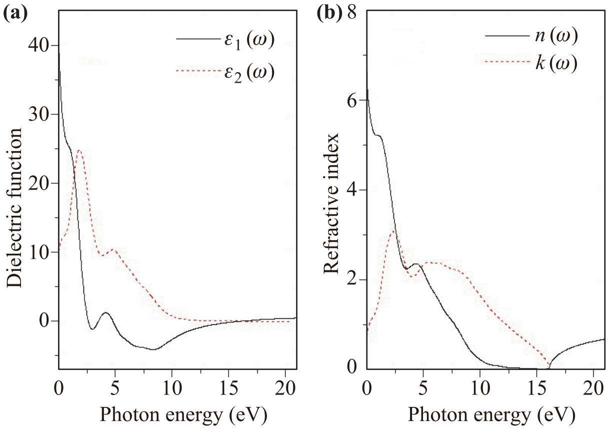

**Fig. 10** Dielectric function **(a)** and refractive index and extinction coefficient **(b)** of $Cr_2AlB_2$.

Figure 11 shows the energy loss function, reflectivity, optical conductivity, and absorption of $Cr_2AlB_2$. From Fig. 11(a), the reflectivity reaches a maximum of 0.96512 at 15.3 eV, followed by a sharp decline with increasing photon energy. In the range of 9.08–16.13 eV, where the reflectivity of $Cr_2AlB_2$ exceeds 70% and the refractive index $n$ of $Cr_2AlB_2$ is smaller, $Cr_2AlB_2$ exhibits the reflective behavior of a metal with high reflectivity. The

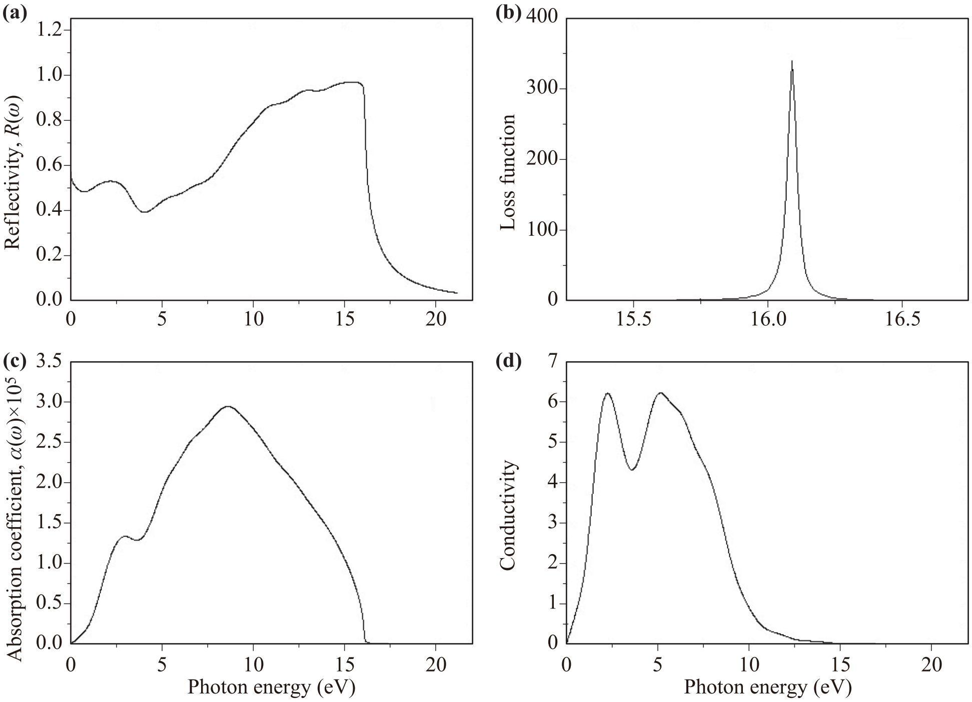

**Fig. 11** Reflectivity **(a)**, energy loss function **(b)**, absorption coefficient **(c)**, and optical conductivity **(d)** of $Cr_2AlB_2$.

lower reflectivity of $Cr_2AlB_2$ at photon energies of 18–22 eV reveals that $Cr_2AlB_2$ is optically transparent in this photon energy range. Figure 11(b) shows the electronic energy loss function of $Cr_2AlB_2$. The energy loss function reaches a maximum at a photon energy of 16.09 eV, which corresponds to the bulk plasma frequency $\omega_p$ of $Cr_2AlB_2$ and is related to plasma oscillation. Note that the $\omega_p$ value of $Cr_2AlB_2$ is nearly equal to its intrinsic oscillation frequency. If the incident light has a frequency greater than the plasma frequency of $Cr_2AlB_2$, the material will be transparent, and its response will change from metallic to dielectric.

Figure 11(c) shows the absorption coefficient of $Cr_2AlB_2$, which reaches the first peak of $1.33287 \times 10^5$ $\mathrm{cm}^{-1}$ at a photon energy of 3.0079 eV and reaches a maximum of $2.93524 \times 10^5$ $\mathrm{cm}^{-1}$ at a photon energy of 8.6225 eV. This indicates that the frequency range of 3.095–15.095 eV is the strongest absorption zone for $Cr_2AlB_2$. From Fig. 11(d), the optical conductivity of $Cr_2AlB_2$ in the photon energy range of 18–22 eV is zero. The optical conductivity reaches a maximum at a photon energy of approximately 2.3 eV, which is close to the peak of the extinction coefficient. At zero photon energy, the optical conductivity is zero because of the zero band gap of the material.

## 4 Conclusion

On the basis of DFT within the GGA, the structural, optical, and thermal properties of $Cr_2AlB_2$ were investigated. Analysis of the elastic constant and phonon dispersion indicated that $Cr_2AlB_2$ is mechanically and thermodynamically stable. Similar to other MAX phases, $Cr_2AlB_2$ exhibits metallic conductivity, according to analysis of the band structure and DOS. The thermal properties at different temperatures and pressures were calculated. The bulk modulus decreases linearly with increasing temperature for $T > 150$ K and increases with increasing pressure at a given temperature. With increasing pressure, the thermal expansion coefficient $\alpha$ decreases sharply for a given temperature. Analysis of the optical properties revealed a large static dielectric constant, indicating that $Cr_2AlB_2$ is a promising dielectric material and is useful in the manufacture of high-value capacitors. At photon energies of 2.66–3.54 eV and 4.82–16.09 eV, light cannot propagate, and $Cr_2AlB_2$ exhibits the reflective behavior of a metal. The strongest absorption of $Cr_2AlB_2$ appears at 3.095–15.095 eV.

**Acknowledgements** This work was supported by the National Natural Science Foundation of China (Grant No. U1304111), the Program for Science & Technology Innovation Talents in Universities of Henan Province (Grant No. 14HASTIT039), and the Innovation Team of Henan University of Science and Technology (Grant No. 2015XTD001).

## References

1. M. W. Barsoum, The $M_{n+1}AX_n$ phases: A new class of solids, *Prog. Solid State Chem.* 28(1–4), 201 (2000)
2. P. Eklund, M. Beckers, U. Jansson, H. Hogberg, and L. Hultman, The $M_{n+1}AX_n$ phases: Materials science and thin-film processing, *Thin Solid Films* 518(8), 1851 (2010)
3. W. Jeitschko, Die Kristallstruktur von MoAlB, *Monatshefte für Chemie und verwandte Teile anderer Wissenschaften*, 97, 1472(1966)
4. W. Jeitschko, The crystal structure of $Fe_2AlB_2$, *Acta Crystallogr. B* 25(1), 163 (1969)
5. H. Y. Chung, M. B. Weinberger, J. B. Levine, A. Kavner, J. M. Yang, S. H. Tolbert, and R. B. Kaner, Synthesis of ultra-incompressible superhard rhenium diboride at ambient pressure, *Science* 316(5823), 436 (2007)
6. P. Rogl, in: Inorganic Reactions and Methods, edited by A. Hagen, New York: Wiley, 1991
7. A. J. Jr Frueh, Confirmation of the structure of chromium boride, CrB, *Acta Crystallogr.* 4(1), 66 (1951)
8. Y. B. Kuz'ma, Crystal structure of the compound $YCrB_4$ and its analogs, *Sov. Phys. Crystallogr.* 15, 312 (1970)
9. Y. B. Kuz'ma and P. I. Krypyakevich, Crystal structure of $Cr_3AlB_4$, *Dopovidi Akademii Nauk Ukrains'koi RSR, Seriya A-Fiziko-Tekhnichni ta Matematichni Nauki*, 34, 1118 (1972)
10. M. Ade and H. Hillebrecht, Ternary borides $Cr_2AlB_2$, $Cr_3AlB_4$, and $Cr_4AlB_6$: The first members of the series $(CrB_2)_nCrAl$ with $n = 1, 2, 3$ and a unifying concept for ternary borides as MAB-Phases, *Inorg. Chem.* 54(13), 6122 (2015)
11. P. Pavone, K. Karch, O. Schutt, D. Strauch, W. Windl, P. Giannozzi, and S. Baroni, *Ab Initio* lattice dynamics of diamond, *Phys. Rev. B* 48(5), 3156 (1993)
12. S. Biernacki and M. Scheffler, Negative thermal expansion of diamond and zinc-blende semiconductors, *Phys. Rev. Lett.* 63(3), 290 (1989)
13. G. Kresse and D. Joubert, From ultrasoft pseudopotentials to the projector augmented-wave method, *Phys. Rev. B* 59(3), 1758 (1999)
14. G. Kresse and J. Furthmuller, Efficient iterative schemes for *ab initio* total-energy calculations using a plane-wave basis set, *Phys. Rev. B* 54(16), 11169 (1996)
15. P. J. Stephens, F. J. Devlin, C. F. Chabalowski, and M. J. Frisch, Ab initio calculation of vibrational absorption and circular dichroism spectra using density functional force fields, *J. Phys. Chem.* 98(45), 11623 (1994)

16. L. Pan, T. C. Lu, and R. Su, Study of electronic structure and optical propertise of g-AlON crystal, *Acta Physica Sinica* 61, 027101 (2012)
17. K. Huang, Solid-State Physics, Beijing: Higher Education Press, 1998
18. X. C. Shen, The Spectrum and Optical Property of Semiconductor, Beijing: Science Press, 1992
19. P. Vinet, J. H. Rose, J. Ferrante, and J. R. Smith, Universal features of the equation of state of solids, *J. Phys.: Condens. Matter* 1(11), 1941 (1989)
20. A. Togo, F. Oba, and I. Tanaka, First-Principles calculations of the ferroelastic transition between rutile-type and $CaCl_2$-type $SiO_2$ at high pressures, *Phys. Rev. B* 78(13), 134106 (2008)
21. F. D. Murnaghan, On the theory of the tension of an elastic cylinder, *Proc. Natl. Acad. Sci. USA* 30(12), 382 (1944)
22. M. D. Segall, P. J. D. Lindan, M. J. Probert, C. J. Pickard, P. J. Hasnip, S. J. Clark, and M. C. Payne, First-Principles simulation: Ideas, illustrations and the CASTEP Code, *J. Phys.: Condens. Matter* 14(11), 2717 (2002)
23. S. Wang, X. Yu, J. Zhang, Y. Zhang, L. Wang, K. Leinenweber, H. Xu, D. Popov, C. Park, W. Yang, D. He, and Y. Zhao, Crystal structures, elastic properties, and hardness of high-pressure synthesized $CrB_2$ and $CrB_4$, *J. Superhard Mater.* 36(4), 279 (2014)
24. S. K. R. Patil, S. V. Khare, B. R. Tuttle, J. K. Bording, and S. Kodambaka, Mechanical stability of possible structures of PtN investigated using first-principles calculations, *Phys. Rev. B* 73(10), 104118 (2006)
25. T. Ma, H. Li, X. Zheng, S. Wang, X. Wang, H. Zhao, S. Han, J. Liu, R. Zhang, P. Zhu, Y. Long, J. Cheng, Y. Ma, Y. Zhao, C. Jin, and X. Yu, Ultrastrong boron frameworks in $ZrB_{12}$: A highway for electron conducting, *Adv. Mater.* 29(3), 1604003 (2017)
26. S. F. Pugh, XCII. Relations between the elastic moduli and the plastic properties of polycrystalline pure metals, *The London, Edinbrugh, and Dublin Philosophical Magazine and Journal of Science* 45(367), 823 (1954)
27. X. Q. Chen, H. Y. Niu, D. Z. Li, and Y. Y. Li, Modeling hardness of polycrystalline materials and bulk metallic glasses, *Intermetallics* 19(9), 1275 (2011)
28. W. L. Johnson and A. R. Williams, Structure and properties of transition-metal-metalloid glasses based on refractory metals, *Phys. Rev. B* 20(4), 1640 (1979)
29. A. P. Thakoor, J. L. Lamb, S. K. Khanna, M. Mehra, and W. L. Johnson, Refractory amorphous metallic $(W_{0.6}\,Re_{0.4})_{76}B_{24}$ coatings on steel substrates, *J. Appl. Phys.* 58(9), 3409 (1985)
30. L. Han, S. Wang, J. Zhu, S. Han, W. Li, B. Chen, X. Wang, X. Yu, B. Liu, R. Zhang, Y. Long, J. Cheng, J. Zhang, Y. Zhao, and C. Jin, Hardness, elastic, and electronic properties of chromium monoboride, *Appl. Phys. Lett.* 106(22), 221902 (2015)
31. S. Baroni, S. de Gironcoli, A. Dal Corso, and P. Giannozzi, Phonons and related crystal properties from density-functional perturbation theory, *Rev. Mod. Phys.* 73(2), 515 (2001)
32. P. Debye, Zur Theorie der spezifischen Wärmen, *Ann. Phys.* 344(14), 789 (1912)
33. A. T. Petit and P. L. Dulong, Recherches Sur quelques points importans de la theorie de la chaleur, *Annales de chimie et de physique* 10, 395 (1819)
34. M. D. Lokman Ali and M. D. Zahidur Rahaman, The Structural, elastic, electronic and optical properties of cubic perovskite $SrVO_3$ compound: An *ab initio* study, *International Journal of Materials Science and Applications* 5(5), 202 (2016)
35. C. L. Li, H. Wang, B. Wang, and R. Wang, First-principles study of the structure, electronic, and optical properties of orthorhombic $BiInO_3$, *Appl. Phys. Lett.* 91(7), 071902 (2007)
36. H. Wang, B. Wang, Q. K. Li, Z. Y. Zhu, R. Wang, and C. H. Woo, First-principles study of the cubic perovskites $BiMO_3$ (M = Al, Ga, In, and Sc), *Phys. Rev. B* 75(24), 245209 (2007)
37. M. Q. Cai, Z. Yin, and M. S. Zhang, First-principles study of optical properties of barium titanate, *Appl. Phys. Lett.* 83(14), 2805 (2003)
38. M. Xu, S. Y. Wang, G. Yin, J. Li, Y. X. Zheng, L. Y. Chen, and Y. Jia, Optical properties of cubic $Ti_3N_4$, $Zr_3N_4$ and $Hf_3N_4$, *Appl. Phys. Lett.* 89(15), 151908 (2006)
39. M. D. Rahman, M. Z. Rahaman, and M. A. Rahman, The structural, elastic, electronic and optical properties of MgCu under pressure: A first-principles study, *Int. J. Mod. Phys. B* 30(27), 1650199 (2016)